

Internal resistance of rear totally diffused solar cells with line shaped contacts

Sebastian Meier,^{1,a)} Pierre Saint-Cast,¹ Nico Wöhrlé,¹ Andreas Fell,¹ Johannes Greulich,¹ Andreas Wolf,¹ and Stefan W. Glunz^{1,2}

¹Fraunhofer Institute for Solar Energy Systems (ISE), Heidenhofstraße 2, 79110 Freiburg, Germany

²Laboratory for Photovoltaic Energy Conversion, University Freiburg, Freiburg, Germany

(Received 10 August 2017; accepted 16 October 2017; published online 10 November 2017)

We present an analytical model for the internal resistance of passivated emitter and rear totally diffused (PERT) solar cells. First, we apply the model of Saint-Cast for the spreading resistance of a passivated emitter and rear cell (PERC) structure with line-shaped contacts. To account for the additional vertical current flow through the silicon wafer and the lateral current flow through the back surface field of a PERT structure, we add a parallel current path using common analytical expressions. We compare the analytical models with two-dimensional numerical simulations based on Quokka 3 and find deviations of less than 6% for the internal resistance. In addition, we compare the analytical model of the internal resistance of PERC and PERT solar cells with experimental data of the series resistance of PERC and PERT solar cells. *Published by AIP Publishing.*

<https://doi.org/10.1063/1.4999685>

I. INTRODUCTION

The passivated emitter and rear cell (PERC)¹ concept is about to become the new industrial standard in photovoltaics. Recently, conversion efficiencies of over 22.5%² and 22% in production³ have been reported. One way to improve the performance of a PV module based on conventional PERC solar cells is the development of bifacial PERC solar cells and first bifacial PERC modules have been presented by integrated manufacturers.^{4,5} A close relative to the PERC solar cell, the passivated emitter and rear totally diffused (PERT) solar cell, opens up interesting opportunities for bifacial solar cells, as the increasing lateral conductance of the boron doped back surface field (BSF) allows decreasing shading by the Al grid on the rear. Until now, first manufacturers produce PERT solar cells based on n-type doped Czochralski-grown silicon (Cz-Si) wafers.⁶ Depending on the process sequence to form emitter and BSF, cell efficiencies around $\eta = 20\%$ are common, with 21% being top of the line.^{7,8} In the case of PERT solar cells based on p-type silicon, the SCHMID Group offers a suitable process sequence.⁹ In 2016, we presented a first co-diffused monofacial PERT solar cell with a peak efficiency of 20.5%.¹⁰ In 2017, Fellmeth *et al.* developed a first bifacial p-type PERT solar cell based on co-diffusion with a peak efficiency of 20.5%.¹¹

The advantage of a bifacial PERT solar cell compared to a bifacial PERC solar cell is as follows: The full area boron doped BSF of the PERT cell offers additional lateral conductance and thus allows for significantly higher rear finger spacing, which will increase the bifaciality of a PERT solar cell compared to a PERC solar cell due to increased rear side carrier generation. In addition, due to the increased conductivity of the BSF, it is possible to use wafers with higher base resistivity. These wafers are less prone to light

induced degradation (LID) due to boron-oxygen complex recombination.¹²

Analytical modeling is a fast and easy way to describe cell structures with local rear contacts.^{13–16} Currently, such models describe PERC structures quite well.^{13,17,18} However, for devices that exhibit a large area BSF, like PERT cells, analytical or empirical expression for the internal resistance is restricted to non-illuminated conditions.¹⁹ The resistance model developed by Saint-Cast¹⁸ is frequently used to describe the spreading resistance of PERC type solar cells with line-shaped contacts for illuminated conditions. In this work, we introduce a model that describes the internal resistance of PERT structures by a parallel connection of the spreading resistance and a resistance, which takes into account the vertical current flow through the Si-wafer and the lateral current flow in the BSF of the PERT cell, which is invariant to the doping type of the solar cells. For verification of the model, we simulate PERC and PERT cells using Quokka 3²⁰ and characterize the total resistance for various combinations of base resistivity, BSF sheet resistance, and line contact pitch. We define the internal resistance as resistance within the Si wafer and the BSF in the case of PERT cells. To avoid any influence of additional external resistance, we set the specific contact resistance of the front and the rear side to negligible small values of $\rho_c = 0.1 \text{ m}\Omega\text{cm}^2$. In the end, we will show that it is possible to account for specific contact resistance by adding this resistance as series connection to the described model. Finally, we compare the analytical model to measurements of the series resistance R_s of p-type Cz-Si PERT solar cells, which have been presented previously.^{10,11}

II. MODEL OF INTERNAL RESISTANCE FOR PERT SOLAR CELLS

In this section, we introduce an analytical model for the internal resistance for PERT solar cells that is valid under

^{a)}Email: sebastian.meier@ise.fraunhofer.de. Tel.: +49 761 4588 5059

illuminated conditions. It combines two current paths through the PERT cell. The first part, addressed in Subsection II A, discusses the existing spreading resistance model of Saint-Cast,¹⁸ which describes a PERC structure with line shaped rear contacts. In Subsection II B, we describe the additional current flow for a PERT cell, where the current flows vertically through the Si-wafer and laterally in the BSF. Finally, in Subsection II C, we present a general analytical model for the description of the internal resistance of PERT type solar cells, which is based on a parallel connection of the resistance models described in Subsections II A and II B.

A. Spreading resistance of PERC solar cells

Figure 1 shows a sketch of a PERC structure with the related geometric parameters. The resulting internal resistance of the base is described as the spreading resistance R_{SP} . It is affected by the thickness W and the base resistivity ρ_b of the Si-wafer, the contact opening width b of the local line-shaped contacts on the rear side of the Si-wafer and the distance (pitch) L_P between two line contacts. All considered models, which are used for describing the internal resistance of PERC and PERT cells, are based on the assumption of flat contacts. In the case of aluminum alloyed contacts on the rear side of PERC and PERT cells, this assumption is invalid due to deep, rather elliptically shaped contacts,²¹ and thus, the model has to be adapted.¹⁹

In the illuminated case, the boundary condition consists of a homogeneous current density distribution at the front side of the sample, caused by the homogeneous illumination. In contrast to other analytical models, this case is well described by the spreading resistance model by Saint-Cast,¹⁸ which reads

$$R_{SP} = \frac{\rho_b b}{2} \left(37f - 2 - \frac{0.3}{f} \right) + \frac{2.82W^{0.88}f^{0.64}}{\tanh(2.82W^{0.88}f^{0.64})} \text{asym}_0 + \text{asym}_\infty, \quad (\text{II.1})$$

with

$$\text{asym}_0 = \frac{\rho_b b^2}{12W} \left(\frac{1}{f} - 1 \right)^2 \quad (\text{II.2})$$

and

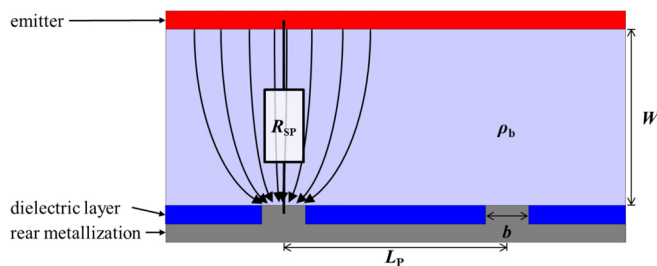


FIG. 1. Sketch of a PERC cross section and relevant geometric parameters. The front side consists of an emitter region. On the rear side, the dielectric passivation layer is locally opened and the Si wafer is contacted by the line shaped contact. The spreading current from the front emitter to the locally contacted rear side is visualized.

$$\text{asym}_\infty = \rho_b W, \quad (\text{II.3})$$

where $f = \frac{b}{L_P}$ is the metallization ratio, $w = \frac{2W}{b}$ is the normalized sample thickness, asym_0 is the case of infinitesimal thin samples ($w \rightarrow 0$), and asym_∞ is the limit of thick samples ($w \rightarrow \infty$). Saint-Cast defines the model valid for metallization ratios $f < 10\%$.

B. Highly doped BSF PERT solar cell

For the limiting case of the PERT cell with a highly doped BSF, we assume the current flow to be strictly vertical in the base and lateral in the rear BSF (see sketch in Fig. 2). This limiting case is only intended as a close approximation of the true current paths if the sheet resistance of the BSF is negligible compared to the sheet resistance of the base $\frac{\rho_b}{W}$.

The equivalent circuit diagram consists of a series connection of the resistance in the bulk of the Si-wafer R_b and the resistance in the boron doped BSF R_{BSF} . For a constant homogeneous current density distribution at the front side, the area-specific resistance through the wafer can be described as

$$R_b = \rho_b W. \quad (\text{II.4})$$

The resistance due to lateral current transport in the BSF layer is calculated equivalent to the well-known case of the emitter resistance.²² It is then given by

$$R_{Lat} = \frac{R_{sh,BSF}}{3} \cdot \frac{(L_P - b)}{2l}, \quad (\text{II.5})$$

with $R_{sh,BSF}$ the sheet resistance of the BSF and l the length of the unit cell along the line contact. The area specific resistance then reads

$$R_{BSF} = R_{Lat} \frac{L_P}{2} l = \frac{R_{sh,BSF} L_P (L_P - b)}{12}. \quad (\text{II.6})$$

C. General model for PERT solar cells

In order to develop a general model for the internal resistance of PERT solar cells, we combine the current paths of a PERC solar cell (see Sec. II A) and the current path through the BSF of a PERT solar cell (see Sec. II B) to a parallel connection of these two current paths. In order to show the current paths and the equivalent circuit, Fig. 3 presents a cross-sectional sketch of a PERT solar cell.

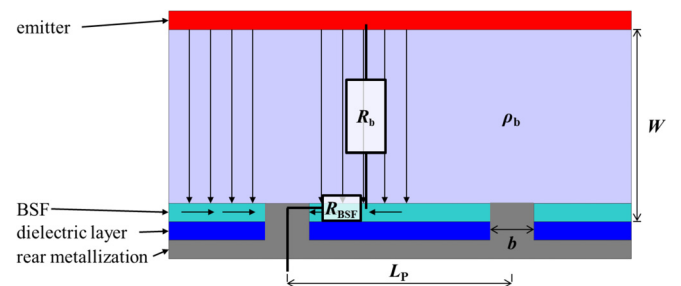


FIG. 2. Schematic of the geometric parameters and equivalent circuit diagram in case of a PERT cell and a current path through the wafer and the BSF.

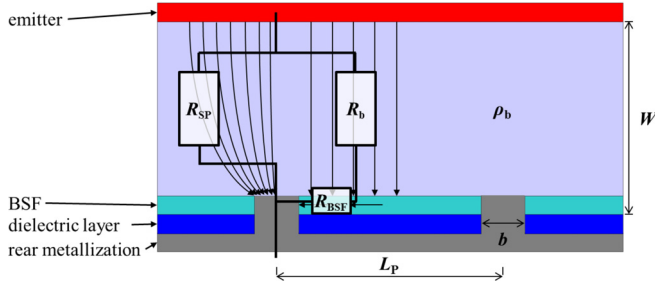


FIG. 3. Schematic of the geometric parameters and equivalent circuit diagram in the case of a PERT type solar cell.

The equivalent circuit diagram consists of a parallel connection between two cases. The first case represents the internal resistance of a PERC solar cell, which is represented by the spreading resistance R_{sp} . The second case describes a PERT solar cell with a current flow through the highly doped BSF which can be expressed as a series connection between the resistance in the Si wafer R_b and the resistance in the BSF R_{BSF} . The total internal resistance R_{int} of a PERT solar cell then reads

$$R_{int} = \left[\frac{1}{R_{sp}} + \frac{1}{R_b + R_{BSF}} \right]^{-1}. \quad (\text{II.7})$$

III. VERIFICATION OF THE ILLUMINATED CASE USING QUOKKA SIMULATIONS

We use the double light method in the Quokka 3 simulations to determine the series resistance R_s .^{23–25} If the IV curve is measured at two different illumination intensities with small change in illumination intensity, the current path and operating condition of the solar cell are invariant. The two illumination intensities result in two shifts of the IV curve, i.e., shift in voltage ΔV and shift in photo generated current Δj_{ph} . The series resistance R_s then reads

$$R_s = \frac{\Delta V}{\Delta j_{ph}}. \quad (\text{III.1})$$

A. Quokka simulation

In order to characterize and verify the developed analytical models for PERC and PERT solar cells, we perform numerical simulations of these solar cells under illumination using Quokka 3.²⁰ Quokka 3 is a numerical simulation tool based on finite element analysis calculating the silicon bulk as a quasi-neutral region. The front and rear side of a solar cell is defined as a skin. A skin layer is a homogeneous area covering everything between the quasi-neutral Si bulk and either the actual surface or the contact to the metal. Skins can be defined as contacted or non-contacted areas. Figure 4 shows a part of a unit cell of a PERT solar cell defined in Quokka 3.²⁰ The rear side of the unit cell consists of a BSF layer, which is contacted locally with line shaped contacts. For the simulation of PERC solar cells, we define the rear skin as passivated skin without lateral conductivity. The front side of the unit cell is contacted by a full area contact which is defined as completely transparent to the incoming light, to avoid any lateral current flow in the emitter. Optical

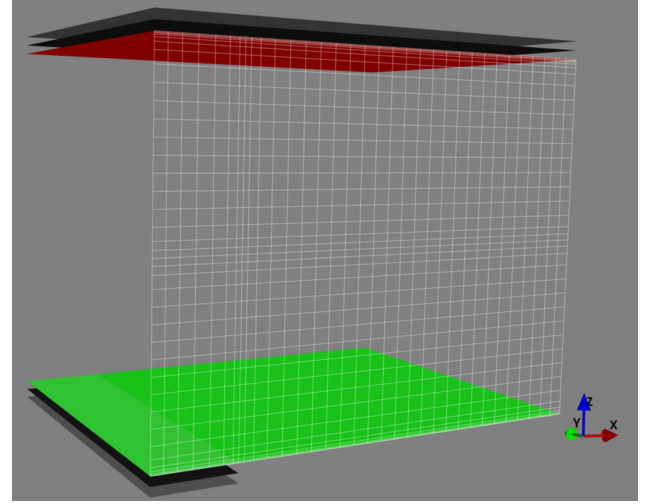


FIG. 4. Unit cell of a PERT solar cell defined in Quokka 3. The rear side consists of a BSF layer and is contacted locally with line shaped contacts. In case of a PERC solar cell, the rear side consists of a passivated skin without lateral conductivity. The front side of the unit cell is fully contacted with a full area metallization which is defined as completely transparent to the incoming light.

parameters and the generation rate are used as proposed in Ref. 26. We determine the series resistance by the double light method.^{23,24}

Typical values for PERC are base resistivities ρ_b between 1 and 3 Ωcm , while PERT ranges between 2 and 6 Ωcm . Covering that, we simulate p-type Cz-Si based PERC and PERT solar cells with a base resistivity ranging from $\rho_b = 1 \Omega\text{cm}$ to 6 Ωcm . In the case of PERT solar cells, we define a boron doped BSF with sheet resistances of $R_{sh,BSF} = 25 \Omega/\text{sq}$ to 200 Ω/sq . The PERC solar cells are defined without BSF. For both concepts, we define locally line shaped rear contacts with distances ranging from $L_p = 0.5 \text{ mm}$ to 2.5 mm. In order to characterize the internal resistance of these solar cells, we set the contact resistance of the front and the rear side metallization to a negligibly small value of $\rho_c = 0.1 \text{ m}\Omega\text{cm}^2$. An overview of the variation of the important parameters is given in Table I.

TABLE I. Important input parameters of the Quokka 3 simulation used in this work.

Parameter	Value	Unit	Description
$\rho_{c,\text{front}}$	0.1	$\text{m}\Omega\text{cm}^2$	Specific contact resistance on the front side
$R_{sh,\text{emitter}}$	90	Ω/sq	Sheet resistance of the emitter
ρ_b	0.5–10	Ωcm	Base resistivity
$R_{sh,BSF}$	25–200	Ω/sq	Sheet resistance of the BSF
$\rho_{c,\text{rear}}$	0.1; 3	$\text{m}\Omega\text{cm}^2$	Specific contact resistance on the rear side
L_p	0.5–2.5	mm	Finger distance on the rear side
b	90	μm	Contact width on the rear side
W	200	μm	Thickness of the solar cell
$J_{0e,\text{pass}}$	100	fA/cm^2	Emitter dark saturation current density
$J_{0e,\text{met}}$	500	fA/cm^2	Emitter dark saturation current density under metallization
$J_{0,BSF,\text{pass}}$	25	fA/cm^2	Passivated BSF dark saturation current density
$J_{0,BSF,\text{met}}$	500	fA/cm^2	BSF dark saturation current density under metallization
$\tau_{\text{SRH,Bulk}}$	500	μs	SRH life time of the Si wafer

B. Comparison between simulation and model

First, the simulated internal resistance for PERC solar cells is compared to the analytical model of the spreading resistance. Figure 5 presents the simulated spreading resistance R_{SP} for solar cells with base resistivity $\rho_b = 0.5, 1, 3$, and $6 \Omega\text{cm}$ and a wafer thickness $W = 200 \mu\text{m}$ as a function of the contact pitch L_p . The simulated data are compared to the model from Eq. (II.1).

Comparing the behavior of spreading resistance R_{SP} over pitch L_p , one can see that the total resistance increases with increasing L_p for PERC solar cells for all base resistivities. In general, the analytical model is in excellent agreement with the numerical results, yielding a root mean square error of $\text{RMSE} = 0.03 \Omega\text{cm}^2$ for all data shown in Fig. 5. The analytical model improves ($\text{RMSE} = 0.02 \Omega\text{cm}^2$) for base resistivities $\rho_b \geq 3 \Omega\text{cm}$ and $L_p \leq 2 \text{ mm}$ if the excess carrier density is taken into account. In this case, an effective base resistivity

$$\rho_{b,\text{eff}} = \frac{1}{\sigma} = \frac{1}{q(\mu_p(N_A + \Delta n) + \mu_n \Delta n)}, \quad (\text{III.2})$$

with the elementary charge q , the concentration of acceptor atoms N_A and the injection and doping-dependent mobility μ_p (holes) and μ_n (electrons) from Refs. 27 and 28.

The excess carrier density Δn at maximum power point MPP reads

$$\Delta n = -\frac{N_A}{2} + \sqrt{\left(\frac{N_A}{2}\right)^2 + n_i^2 \exp\left(\frac{V_{\text{MPP}}}{V_{\text{th}}}\right)}, \quad (\text{III.3})$$

with the voltage at MPP V_{MPP} and the thermal voltage $V_{\text{th}} = \frac{k_B T}{q}$. For each resistivity ρ_b , the average value of V_{MPP}

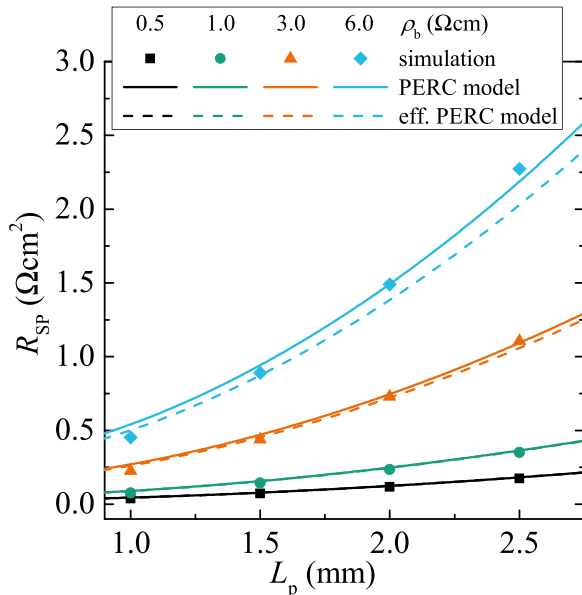


FIG. 5. Simulated spreading resistance R_{SP} over L_p for PERC solar cells with base resistivity of $\rho_b = 0.5 \Omega\text{cm}$ (black squares), $\rho_b = 1 \Omega\text{cm}$ (green circles), $\rho_b = 3 \Omega\text{cm}$ (orange triangles) and $\rho_b = 6 \Omega\text{cm}$ (blue diamonds). The simulated data are compared to the model from Eq. (II.1) (solid lines). The analytical model in dashed lines takes the excess carrier density and thus an effective base resistivity $\rho_{b,\text{eff}}$ into account.

for all the simulations with L_p between 0.5 mm and 2.5 mm is considered. Thus, we consider majority and minority carriers for the calculation of the excess conductivity. This decreases the total resistance R_{int} resulting in a good agreement with the simulated data. However, in case of $\rho_b = 6 \Omega\text{cm}$ and $L_p > 2.0 \text{ mm}$, the RMSE increases to $\text{RMSE} = 0.06 \Omega\text{cm}^2$. This deviation for high L_p of the model from the simulated data was already observed by other authors.^{21,29}

The analogous simulation set is performed in case of PERT cells (see Fig. 6). In the graph, one can compare the simulated data with the analytical model developed in Sec. II C [Eq. (II.7)]. The graph shows the total resistance of PERT solar cells with sheet resistance of the BSF of $R_{\text{sh,BSF}} = 25 \Omega/\text{sq}$ (top left), $R_{\text{sh,BSF}} = 50 \Omega/\text{sq}$ (top right), $R_{\text{sh,BSF}} = 100 \Omega/\text{sq}$ (bottom left) and $R_{\text{sh,BSF}} = 200 \Omega/\text{sq}$ (bottom right) as a function of L_p for $\rho_b = 0.5, 1, 3$, and $6 \Omega\text{cm}$.

In every case of sheet resistance of the BSF, R_{int} increases with increasing pitch L_p . It ranges from $R_{\text{int}} = 0.008 \Omega\text{cm}^2$ at $R_{\text{sh,BSF}} = 25 \Omega/\text{sq}$, $L_p = 0.5 \text{ mm}$ and $\rho_b = 0.5 \Omega\text{cm}$ to $R_{\text{int}} = 0.707 \Omega\text{cm}^2$ at $R_{\text{sh,BSF}} = 200 \Omega/\text{sq}$, $L_p = 2.5 \text{ mm}$ and $\rho_b = 6 \Omega\text{cm}$. In general, the analytical model developed in Eq. (II.7) shows good agreement with the simulated PERT solar cells, which results in a low value of $\text{RMSE} = 0.02 \Omega\text{cm}^2$. The analytical model overestimates the simulated results slightly. The deviation between analytical model and simulated data can be decreased if the excess carrier density is taken into account. For $\rho_b = 6 \Omega\text{cm}$, the excess carrier density is approximately 10% of the carrier density resulting from the base resistivity of the Si wafer. The effective base resistivity reduces R_{int} , which leads to an improvement of the model resulting in low RSME ($0.01 \Omega\text{cm}^2$) for all simulated parameters. This corresponds to a decrease in RSME of 50% compared to the analytical model based on the base resistivity without respect to the excess carrier density. Comparing the y-scale of plots in Figs. 5 and 6 shows that in the case of $\rho_b \geq 3 \Omega\text{cm}$ and $R_{\text{sh,BSF}} \leq 200 \Omega/\text{sq}$, the internal resistance of the PERT structure is a factor of 2 to 10 lower than that for the corresponding PERC structure. Thus, in almost all cases of PERT cells shown in Fig. 6, the current path through base and BSF (Fig. 2) is dominating.

In the following, we will discuss the resistance in a PERT solar cell due to the current path described in Sec. II B, meaning a vertical current flow through the bulk wafer and a lateral current flow in the BSF. In order to extract the resistance $R_b + R_{\text{BSF}}$ [see Eqs. (II.4) and (II.6)], we perform simulations of PERC and PERT solar cells. Based on the general model of the internal resistance of PERT solar cells in Eq. (II.7), the spreading resistance R_{SP} can be extracted by the numerical simulation of the internal resistance of a PERC, which we call $R_{\text{int,PERC}}$. In addition, we numerically simulate a PERT solar cell to extract the corresponding value $R_{\text{int,PERT}}$. In a simplified approach, the resistance due to current path in the bulk and in the BSF can be extracted by simulation assuming a parallel connection

$$R_b + R_{\text{BSF}} = \left[\frac{1}{R_{\text{int,PERT}}} - \frac{1}{R_{\text{int,PERC}}} \right]^{-1}. \quad (\text{III.4})$$

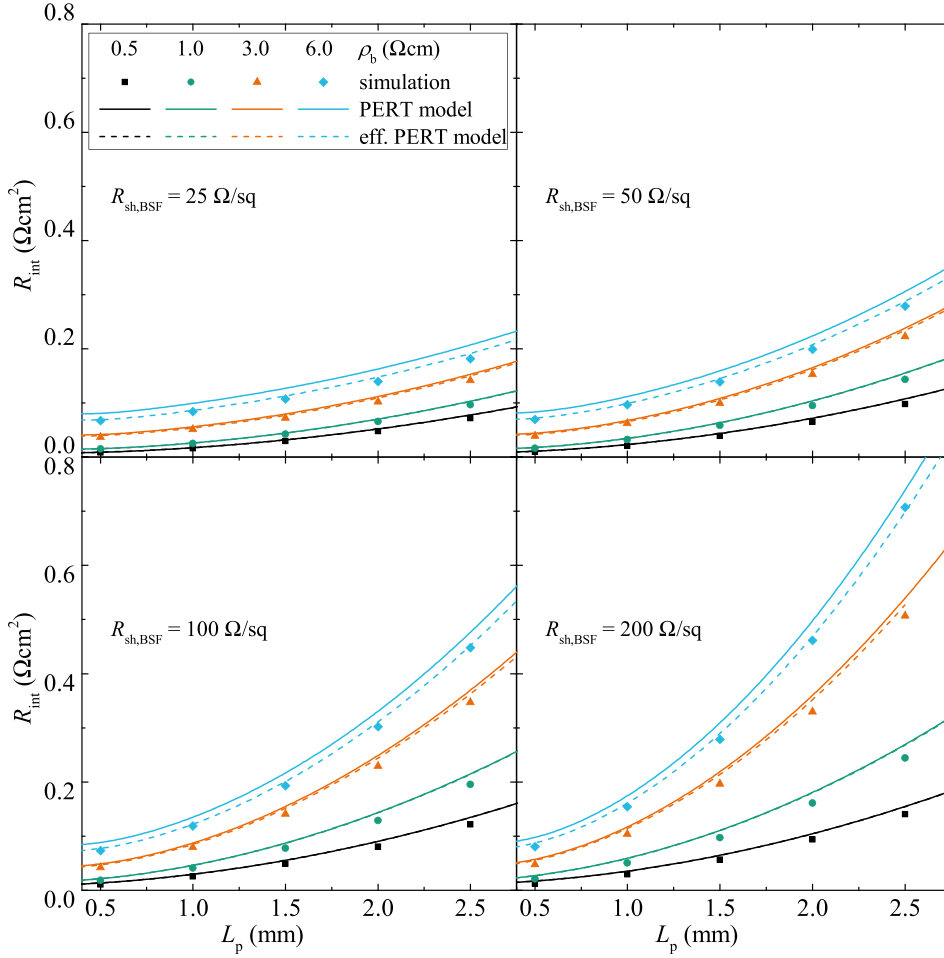


FIG. 6. Simulated total resistance R_{int} over L_p for PERT solar cells with $R_{\text{sh,BSF}} = 25 \Omega/\text{sq}$ (top left), $50 \Omega/\text{sq}$ (top right), $100 \Omega/\text{sq}$ (bottom left), and $200 \Omega/\text{sq}$ (bottom right). The base resistivity ranges from $\rho_b = 0.5 \Omega\text{cm}$ (black squares), $\rho_b = 1 \Omega\text{cm}$ (green circles), $\rho_b = 3 \Omega\text{cm}$ (orange triangles) to $\rho_b = 6 \Omega\text{cm}$ (blue diamonds). The simulated data are compared with the model from Eq. (II.7) (solid lines). The analytical models in dashed lines apply the effective resistivity $\rho_{b,\text{eff}}$.

Figure 7 shows the comparison between the simulated value of Eq. (III.4) and the analytical expressions of Eqs. (II.4) and (II.6) for $R_{\text{sh,BSF}} = 25 \Omega/\text{sq}$.

The resistance due to the current path through the bulk and the BSF $R_b + R_{\text{BSF}}$ increases independently from the base resistivity with increasing pitch. The model shows good agreement with the simulated resistance $R_b + R_{\text{BSF}}$ for low $\rho_b = 0.5 \Omega\text{cm}$ and $1 \Omega\text{cm}$ with a maximum deviation of $\text{RMSE} = 0.005 \Omega\text{cm}^2$. Increasing the pitch increases the deviation of the analytical model. Since the conductivity of the bulk wafer is high with $\rho_b = 0.5 \Omega\text{cm}$ and $1 \Omega\text{cm}$, one cannot see a difference in the resistance if the excess carrier density is taken into account. The situation changes with increasing base resistivity. In the case of PERT with $\rho_b = 3 \Omega\text{cm}$ and $6 \Omega\text{cm}$, the excess carrier density has a big influence on the resistance, since it affects strongly the base resistivity for higher values of ρ_b . Quantitatively, this can be seen in the RMSE of the two models. In the case of a base resistivity of $\rho_b = 6 \Omega\text{cm}$, the agreement of the analytical model is characterized by $\text{RMSE} = 0.02 \Omega\text{cm}^2$. The effective base resistivity decreases in this case to $\rho_{b,\text{eff}} = 5.1 \Omega\text{cm}$, which leads to a decrease in the resistance $R_b + R_{\text{BSF}}$ and thus to a better agreement with the simulation. This results in RMSE of $\text{RMSE} = 0.007 \Omega\text{cm}^2$. In the following, we will discuss the deviation with increasing pitch.

Figure 8 presents the resistance $R_b + R_{\text{BSF}}$ of a PERT solar cell with a sheet resistance of the BSF of $R_{\text{sh,BSF}} = 200 \Omega/\text{sq}$. Again, the simulated resistance increases

with increasing pitch for all base resistivities. The analytical model shows the same behavior, but overestimates the resistance in every case leading to a $\text{RMSE} = 0.07 \Omega\text{cm}^2$. Note that taking into account the effective base resistivity has only

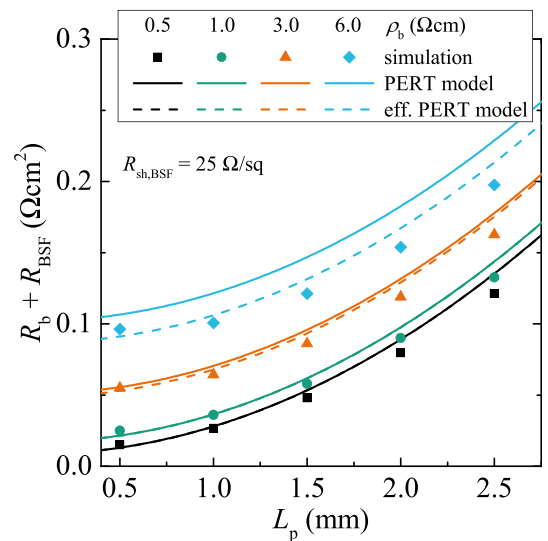


FIG. 7. Simulated resistance $R_b + R_{\text{BSF}}$ over L_p for PERT solar cells with $R_{\text{sh,BSF}} = 25 \Omega/\text{sq}$ and base resistivity of $\rho_b = 0.5 \Omega\text{cm}$ (black squares), $\rho_b = 1 \Omega\text{cm}$ (green circles), $\rho_b = 3 \Omega\text{cm}$ (orange triangles) and $\rho_b = 6 \Omega\text{cm}$ (blue diamonds). The simulated data are compared to the model from Eq. (III.4) (solid lines). The analytical models in dashed lines apply the effective base resistivity $\rho_{b,\text{eff}}$.

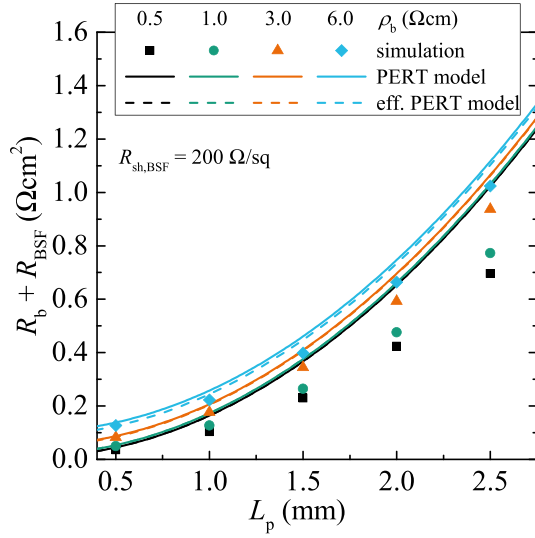


FIG. 8. Simulated resistance $R_b + R_{BSF}$ over L_p for PERT solar cells with $R_{sh,BSF} = 200 \Omega/\text{sq}$ and base resistivity of $\rho_b = 0.5 \Omega\text{cm}$ (black squares), $\rho_b = 1 \Omega\text{cm}$ (green circles), $\rho_b = 3 \Omega\text{cm}$ (orange triangles) and $\rho_b = 6 \Omega\text{cm}$ (blue diamonds). The simulated data are compared to the model (solid lines). The analytical models in dashed lines apply the effective base resistivity $\rho_{b,eff}$.

a small impact on the presented resistance. This is due to the series connection between R_b [Eq. (II.4)] and R_{BSF} [Eq. (II.6)]. In this series connection, high values of sheet resistance in the BSF with $R_{sh,BSF} = 200 \Omega/\text{sq}$ dominate the total resistance. The stronger deviation compared with the case of $R_{sh,BSF} = 25 \Omega/\text{sq}$ demonstrates the limits of the analytical expression. For a higher sheet resistance, the potential gradient within the BSF increases, leading to lateral current components within the wafer bulk.

C. Verification of the internal resistance model of PERT solar cells

In this work, the characterization of the internal resistance of PERT solar cells is performed over a wide range of parameters, namely from $\rho_b = 0.5 \Omega\text{cm}$ to $10 \Omega\text{cm}$, $R_{sh,BSF} = 25 \Omega/\text{sq}$ to $200 \Omega/\text{sq}$ and $L_p = 0.5 \text{ mm}$ to 2 mm resulting in 150 data points. Figure 9 presents a correlation graph with the analytical model based on the parallel connection [Eq. (II.7)]. The analytical model based on the dark resistivity ρ_b (green squares) is in good agreement with the simulated data resulting in low $\text{RMSE}_{\text{total}} = 0.02 \Omega\text{cm}^2$. Nevertheless, the model accuracy improves if the excess carrier density is taken into account by using $\rho_{b,eff}$ (orange triangles). The deviation decreases to $\text{RMSE}_{\text{total}} = 0.01 \Omega\text{cm}^2$, which is a reduction in deviation of 50% over the whole range of parameters. Additionally, we plot in blue circles for selected data points an additional model including contact resistance ρ_c in series using $\rho_c = 3 \text{ m}\Omega\text{cm}^2$ as presented by other authors,^{21,29} the corresponding Quokka simulation applies $\rho_c = 3 \text{ m}\Omega\text{cm}^2$ as well. Again, a very good agreement is observed. Thus, the derived analytical model is also valid, if the contact resistance is not negligible.

Further, we compare our analytical model with experimental data of the series resistance of PERC and PERT solar cells. The experimental details and cell results are described in

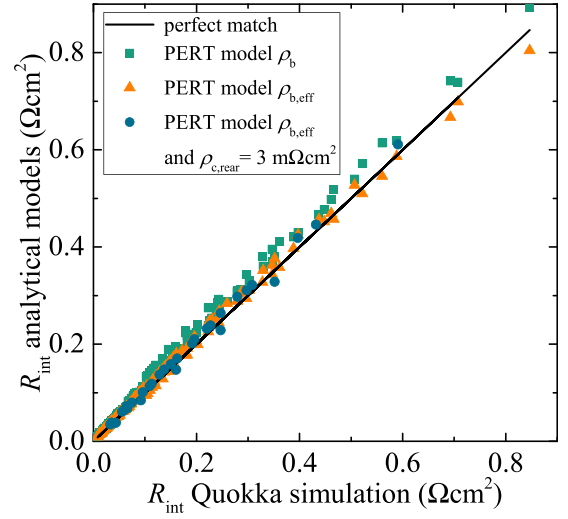


FIG. 9. Correlation graph between Quokka 3 based simulated data for the internal resistance of PERT solar cells with the analytical model developed in this work; see Eq. (II.7). The green squares represent the analytical model using ρ_b as base resistivity. If the excess carrier density is taken into account (orange triangles) by applying $\rho_{b,eff}$, the agreement improves. The blue circles additionally represent the case for an increased rear contact resistance.

Ref. 10. We distinguish between a series resistance that is generated from the front side $R_{s,front}$ (emitter and metallization) and the internal resistance of PERC and PERT solar cells based on the analytical models presented [see Eqs. (II.1) and (II.7)]. We use the Excel-based tool Gridmaster for the calculation of $R_{s,front}$.³⁰ The total calculated series resistance R_s then reads

$$R_s = R_{s,front} + R_{int}. \quad (\text{III.5})$$

Using $\rho_{b,eff}$ for R_{int} , Fig. 10 presents the measured R_s of PERC and PERT solar cells using a conventional IV-tester in function of the calculated series resistance R_s of Eq. (III.5). The R_s is extracted from comparison of a light (STC³¹) and dark IV measurements. The y-error represents the standard deviation of a group of similar processed solar cells. In the

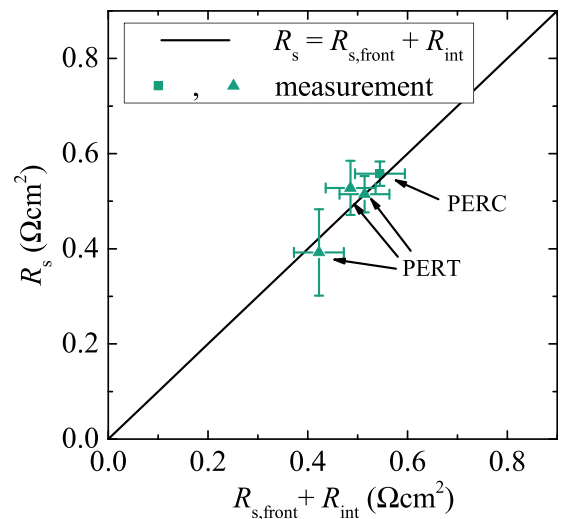


FIG. 10. Measured series resistance R_s of PERC and PERT solar cells using a conventional IV tester over the calculated internal resistance, which consists of the analytical models R_{int} described in this work and the series resistance $R_{s,front}$ of the front side of the solar cells.

case of the calculated series resistance $R_{s,\text{front}} + R_{\text{int}}$, we define the error based on the deviation of the input parameters to calculate $R_{s,\text{front}}$. Due to inhomogeneous emitter formation, the specific contact resistance $\rho_{c,\text{front}}$ varies from 1 to 5 m Ωcm^2 , which has a big influence on $R_{s,\text{front}}$ and leads to an error of $f_{R_{s,\text{front}}} = 0.05 \Omega\text{cm}^2$.

In conclusion, the analytical model for the internal resistance of PERT solar cells shows good agreement with the simulated data using Quokka 3 (see Fig. 9). In Fig. 10, we are able to correlate the calculated series resistance using R_{int} and $R_{s,\text{front}}$ with experimental data extracted from IV measurements of PERC and PERT solar cells. Due to this, we conclude that the presented analytical model is well suited for modeling the internal resistance of PERT solar cells.

IV. SUMMARY AND CONCLUSION

In this paper, we have verified the analytical model for the spreading resistance of a PERC solar cell with line shaped contacts on the rear side, developed by Saint-Cast¹⁸ with numerical device simulations. As already observed by other authors, we find that the model underestimates the internal resistance at large contact distance $L_p > 2$ mm and high resistivity of the base $\rho_b > 6 \Omega\text{cm}$. Based on this model, we have presented an analytical model for the internal resistance of PERT solar cells. This model consists of a parallel connection between two current paths, namely the current path in a PERC solar cell and an additional current path, which consists of a vertical current flow through the Si wafer and a lateral current flow through the BSF.

The analytical models are compared to the internal resistance extracted from numerical simulations, based on a broad variation of base resistivity ρ_b , sheet resistance of the BSF $R_{\text{sh,BSF}}$ and rear finger pitch L_p . In general, the simulated total resistance of PERT solar cells has shown good agreement with the internal resistance models. It is observed that at large pitches the resistance of the PERT current path is overestimated by the internal resistance model, showing the limitations of the analytical model due to the assumption of no lateral voltage gradient in the bulk. Looking closer to the analytical models, it is crucial to take the excess carrier density into account for a more realistic determination of the bulk resistivity. This leads to a decrease in ρ_b and thus to a very good agreement with the numerical model ($\text{RMSE}_{\text{total}} = 0.01 \Omega\text{cm}^2$), especially for high bulk resistivity values. Adding specific contact resistance to the models mentioned in this work is possible by adding them as series connection. We verified the resistance model of PERT solar cells for a rear specific contact resistance of $\rho_{c,\text{rear}} = 3 \text{ m}\Omega\text{cm}^2$. Finally, we have presented experimental data for the resistance of PERT and PERC type solar cells, which confirms the predictions of the model.

ACKNOWLEDGMENTS

This work was funded by the German Federal Ministry for Economic Affairs and Energy within the project “KoKoBi” under Contract No. 0325875B.

S. Meier gratefully acknowledges the scholarship of the “Heinrich Böll Stiftung.”

- ¹A. W. Blakers, A. Wang, A. M. Milne, J. Zhao, and M. A. Green, *Appl. Phys. Lett.* **55**, 1363 (1989).
- ²See <http://ir.trinasolar.com/phoenix.zhtml?c=206405&p=irol-newsArticle&ID=2230468> for Trina Solar Limited press release, Trina Solar Announces New Efficiency Record of 22.61% for Mono-Crystalline Silicon PERC Cell; accessed 02 October 2017.
- ³M. Schaper, J. Cieslak, K. Duncker, C. Fahrland, S. Geissler, S. Hörnlein, C. Klenke, R. Lantzs, A. Mohr, A. Niebergall, A. Schönmann, M. Schütze, J. W. Müller, and D. J. W. Jeong, in 32nd EUPVSEC München (2016).
- ⁴See <http://www.trinasolar.com/en-uk/resources/newsroom/mon-05012017-1500> for Trina Solar Limited press release, Trina Solar launches bifacial PERC Module “DUOMAX Twin;” accessed 02 October 2017.
- ⁵SolarWorld AG press release, SolarWorld will debut 72-cell bifacial solar panel at Solar Power International, <http://www.solarworld-usa.com/newsroom/news-releases/news/2015/solarworld-will-debut-72-cell-bifacial-solar-panel-at-solar-power-international>; accessed 02 October 2017.
- ⁶See http://ir.yinglisolar.com/phoenix.zhtml?c=213018&p=irol-newsArticle_print&ID=2232939 for Yingli Solar press release, Yingli’s PANDA Bifacial Module Receives CGC’s Top Runner Program Certification; accessed 02 October 2017.
- ⁷B. Lim, F. Kiefer, T. Brendemühl, A. Christ, M. Berger, R. Peibst, T. Dullweber, T. Falcon, N. Takeda, and R. Anderson, in nPV Workshop (2014).
- ⁸Z.-W. Peng, P.-T. Hsieh, C.-J. Huang, Y.-J. Lin, P.-K. Chang, C. Kuo, and C.-C. Li, *Energy Procedia* **92**, 702 (2016).
- ⁹See <http://www.nacleanenergy.com/articles/19097/erdm-solar-schmid-group-announce-supply-agreement-for-world-s-first-full-geminus-bifacial-turnkey-cell-module-manufacturing-line-with-multi-bus-bar-module-technology> for SCHMID Group press release, ERDM Solar and SCHMID Group announce the supply agreement for the world’s first full GEMINUS bifacial turnkey cell and module manufacturing line with multi bus bar module Technology.
- ¹⁰S. Meier, S. Wiesnet, S. Mack, S. Werner, S. Maier, S. Unmüßig, C. Demberger, H. Knauss, D. Biro, and A. Wolf, in 32nd EUPVSEC München (2016).
- ¹¹T. Fellmeth, S. Meier, F. Clement, A. Wolf, H. Knauss, and H. Haverkamp, *Energy Procedia* **124**, 875 (2017).
- ¹²K. Bothe, R. Sinton, and J. Schmidt, *Prog. Photovoltaics: Res. Appl.* **13**, 287 (2005).
- ¹³A. Kimmerle, M. Rüdiger, A. Wolf, M. Hermle, and D. Biro, *Energy Procedia* **27**, 219 (2012).
- ¹⁴A. Wolf, D. Biro, J. Nekarda, S. Stumpp, A. Kimmerle, S. Mack, and R. Preu, *J. Appl. Phys.* **108**, 124510 (2010).
- ¹⁵B. Fischer, “Loss analysis of crystalline silicon solar cells using photoconductance and quantum efficiency measurements,” Ph. D. thesis (University of Konstanz, 2003).
- ¹⁶H. Plagwitz, “Surface passivation of crystalline silicon solar cells by amorphous silicon films,” Ph. D. thesis (University of Hanover, 2007).
- ¹⁷A. Fallisch and D. Biro, *IEEE J. Photovoltaics* **1**, 153 (2011).
- ¹⁸P. Saint-Cast, “Passivation of Si surfaces by PECVD aluminium oxide,” Ph. D. thesis (University of Konstanz, 2012).
- ¹⁹S. Meier, S. Unmüßig, A. Brand, P. Saint-Cast, T. Fellmeth, A. Wolf, and S. Glunz, *Energy Procedia* **124**, 881 (2017).
- ²⁰A. Fell, J. Schön, M. C. Schubert, and S. W. Glunz, *Sol. Energy Mater. Sol. Cells* **173**, 128–133 (2017).
- ²¹M. Müller and F. Lottspeich, *J. Appl. Phys.* **115**, 84505 (2014).
- ²²A. Goetzberger, J. Knobloch, and B. Voss, *Crystalline Silicon Solar Cells* (John Wiley & Sons, Ltd., Chichester, UK, 1998).
- ²³M. Wolf and H. Rauschenbach, *Adv. Energy Convers.* **3**, 455 (1963).
- ²⁴K. C. Fong, K. R. McIntosh, and A. W. Blakers, *Prog. Photovoltaics: Res. Appl.* **21**, 490–499 (2013).
- ²⁵D. Pysch, A. Mette, and S. W. Glunz, *Sol. Energy Mater. Sol. Cells* **91**, 1698 (2007).
- ²⁶A. Fell, K. R. McIntosh, P. P. Altermatt, G. Janssen, R. Stangl, A. Ho-Baillie, H. Steinkemper, J. Greulich, B. Min, K. C. Fong, M. Hermle, I. G. Romijn, and M. D. Abbott, *IEEE J. Photovoltaics* **5**, 1250 (2015).
- ²⁷D. B. M. Klaassen, *Solid State Electron.* **35**, 953 (1992).
- ²⁸D. B. M. Klaassen, *Solid State Electron.* **35**, 961 (1992).
- ²⁹C. Kranz, B. Lim, U. Baumann, and T. Dullweber, *Energy Procedia* **67**, 64 (2015).
- ³⁰T. Fellmeth, F. Clement, and D. Biro, *IEEE J. Photovoltaics* **4**, 504 (2014).
- ³¹International Electrotechnical Commission, *Photovoltaic Devices—Procedures for Temperature and Irradiance Corrections to Measured I-V Characteristics* (IEC, 2009).